TABLE OF CONTENTS

LIST OF FIGURES

LIST OF TABLES

CHAPTER 1

Introduction

The acceleration of atomic nuclei to ultra-relativistic energies in recent years has made possible studies of electromagnetic dissociation (EMD) using the virtual photon field of the target nucleus [1-5]. An important advantage of this technique over the experiments using real photons on a target at rest is that the decay products are given large energies through the Lorentz boost, so that they can be identified and measured. In experiment E814, operating at the AGS at Brookhaven National Laboratory, we have seen the full spectrum of decays of ^{28}Si by this method [31]. This thesis describes the measurement of absolute cross sections, and the complete kinematic reconstruction of a few of these decay channels.

A Relativistic Heavy-ion Collisions

The nucleus-nucleus collisions occur mainly through either the strong or the electromagnetic interactions. At relativistic energies, these two interactions can be classified according to the the distance between the colliding nuclei. [1] Figure 1.1 shows an interaction between a projectile nucleus A_P and a target nucleus A_T. The nucleons which undergo inelastic scattering are called participants and the nucleons which do not participate in the collision are called spectators. The impact parameter plays an important role in deciding the ratio between participants and spectators in any given collision. We can separate the interactions into two major classes, namely those with $b < R_P + R_T$ and those with $b > R_P + R_T$. In the collisions with $b < R_P + R_T$, the overlapping nucleons undergo inelastic collisions and the remains of the projectile move forward essentially undisturbed (nuclear fragmentation). The highest degree of centrality in this case could be achieved when $b = 0$ where a maximum number of nucleons will undergo inelastic collisions (central collisions). The collisions with $b > R_P + R_T$ occur mainly via electromagnetic interactions (peripheral collisions).

The peripheral collisions between two heavy ions can occur via two scattering mechanisms, namely Coulomb scattering, which is the interaction of the projectile with the electromagnetic field of the target nucleus, and hadronic scattering, which is the interaction of the projectile and the target either through nucleus-nucleus in-

[1] impact parameter b

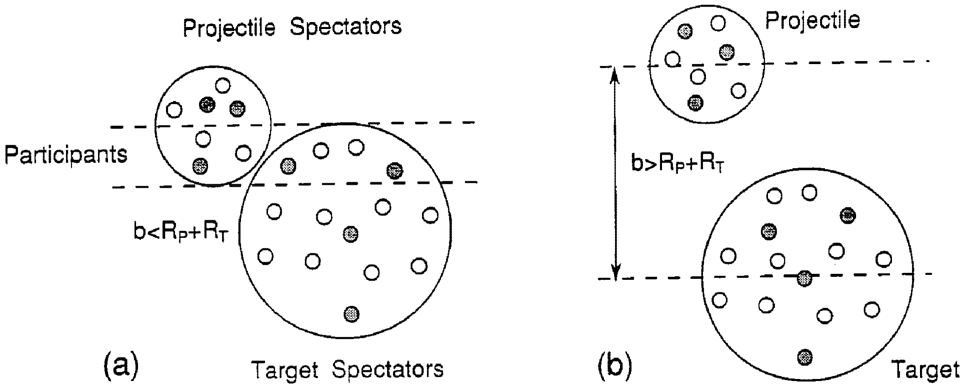

Figure 1.1: Collision between two relativistic heavy ions.

teraction (elastic scattering of the projectile by the target as a whole) or through nucleon-nucleon interaction (inelastic scattering by the individual nucleons at the surface of the colliding nuclei). Both the coulomb and the hadronic scattering can induce excitations in the colliding nuclei, which will decay by emitting either a γ ray or a few nucleons. The differential cross sections of the peripheral heavy ion scattering can be written in the form [6, 7],

$$\frac{d\sigma}{d\Omega} = |f_{coul}(\theta) + f_{had}(\theta)|^2 + \frac{d\sigma_{inel}}{d\Omega}$$

where $f_{coul}(\theta)$ and $f_{had}(\theta)$ are the coulomb and the hadronic elastic scattering amplitudes for the nucleus as a whole and $d\sigma_{inel}/d\Omega$ is the inelastic or quasi-elastic scattering of the individual nucleons at the surface of the colliding nuclei.

The coulomb scattering amplitude for ultra-relativistic energy collisions with heavy ions can exceed the pure geometrical cross section by several orders of magnitude. In addition, at very low momentum transfer collisions, the coulomb scattering becomes the most dominant term, and thus could be used as an experimental tool to select candidates for electromagnetic interactions. The theoretical models behind coulomb scattering will be discussed in more detail in the following section.

The hadronic scattering amplitude, in the presence of a strong coulomb interaction can be described by the behavior of light scattering through a small aperture or the light scattered by a black disk, which has the characteristics of the Fresnel diffraction pattern [8]. This has been observed in heavy ion collisions at low beam energies ranging from a few MeV and extending up to relativistic energies.

The inelastic hadronic scattering of nucleons at the surface of the two colliding nuclei usually induces nuclear fragmentation. This has been observed in nucleon-nucleus (pA) scattering experiments at various beam energies [9].

B Electromagnetic Dissociation

1 Equivalent Photon Method

The equivalent photon method [11] can be considered as the simplest way to describe the reaction mechanism of electromagnetic interactions in relativistic collisions. In the literature, this method is well known as the Weizsäcker-Williams method (WW). A complete description of WW can be found in the textbook of Jackson on classical electrodynamics [10].

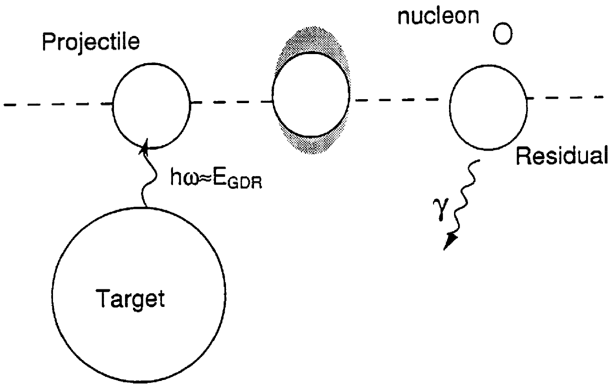

Figure 1.2: Electromagnetic dissociation.

Consider the example shown in Figure 1.2 of a projectile interacting with a target electromagnetic field. In the WW approximation, the target electromagnetic field can be replaced by a flux of virtual photons, and therefore this interaction is equivalent to the absorption of photons by the projectile. For simplicity, the absorption of a single photon is considered. One should notice that the target and the projectile can be interchanged through a Lorentz transformation. The projectile, which contains the excess energy of the absorbed photon, will eventually decay by emitting either a γ ray or a nucleon. The EMD cross section in the WW approximation can be given by

$$\sigma_{EMD} = \int_0^\infty n(\omega)\sigma(\omega)\frac{d\omega}{\omega}$$

where ω is the virtual photon frequency, $n(\omega)$ is the virtual photon flux integrated over all the impact parameters at a given photon energy and $\sigma(\omega)$ is the photonuclear cross section which can be found in the literature [12, 13, 14]. It can be shown that in a collision with impact parameter b, the virtual photon spectrum contains photons with energies up to a maximum value given by $E_\gamma^{max} \approx \gamma(\hbar c/b_{min})$, implying that for a given impact parameter, only excitations up to a certain value can be reached. The virtual photon flux, integrated over all the impact parameters is given by [11],

$$n(\omega) = \frac{2}{\pi} Z_T^2 \alpha \left[\frac{c}{v}\right]^2 \left(\xi K_0(\xi) K_1(\xi) - \frac{v^2\xi^2}{2c^2}\left[K_1(\xi)^2 - K_0(\xi)^2\right]\right) \qquad (1.1)$$

where Z_T is the target charge, $\xi = \omega b_{min}/\gamma v$, $\alpha = e^2/\hbar c$ is the fine structure constant, $K_0(\xi)$ and $K_1(\xi)$ are the modified Bessel functions, and v and γ are the projectile velocity and the Lorentz factor respectively. The value of b_{min} for the coulomb excitation can be taken as the sum of the nuclear radii $R_T + R_P$.

At higher energies where $\gamma >> 1$, it is useful to rewrite the virtual photon spectrum as [11],

$$n(\omega) = \frac{2Z_T^2\alpha}{\pi} \ln\left[\frac{\delta\gamma v}{\omega b_{min}}\right]$$

where $\delta = 0.681$. This simple formula can be used for most practical purposes. It can be seen that the virtual photon spectrum has a simple scaling of $\ln(\gamma)$ and $\ln(1/b_{min})$, both of which modify the naive expectation of Z_T^2 dependance.

Figure 1.3 shows the experimentally measured photo-absorption cross section of the ^{28}Si nucleus as a function of the photon energy [6]. The spectrum shows the response of the nucleus to the photons for energies between 10 MeV and 500 MeV. The peak at 20 MeV corresponds to the excitation of the Giant Dipole Resonance in ^{28}Si. The Giant Dipole resonance arises from an oscillation of the protons with respect to the neutrons in the nucleus. The predicted energy for such oscillations corresponds to $E_{GDR} = 76/A^{1/3}$ MeV for a nucleus with mass A and has been observed experimentally for various light and heavy nuclei. This resonance can be stimulated by photons with wavelengths comparable to the dimensions of the nucleus. The second peak at 300 MeV corresponds to the excitation of the Δ resonance in the nucleus. The region in between the resonances is the quasi-deuteron region. In this region, a dipole consisting of a proton and a neutron, responds to the photon wavelength, which exceeds the dimensions of a single nucleon [6]. For comparison, the virtual photon spectrum generated for three beam momenta is also shown in the same figure for the case in which a ^{28}Si projectile interacts with the electromagnetic field of a ^{208}Pb target. It can be seen from this plot that the AGS energy of 14.6 GeV/nucleon is well suited for the study of the GDR in ^{28}Si. At CERN, the energy of 200 GeV/nucleon creates a photon spectrum which populates other resonance states which can compete with the GDR, while the Bevalac energy of 2.1 GeV/nucleon produces a spectrum which falls quite rapidly over the resonance region.

The early comparisons between the theoretical calculations of the electromagnetic dissociation cross sections obtained from the WW approximation and the experimentally measured cross sections obtained at the Bevalac indicated several discrepancies. This was explained as a difficulty in subtracting the nuclear component from the electromagnetic cross sections [15]. The measurements of the exclusive cross section of ^{28}Si decaying into specific channels containing up to several nucleons were published for the first time by the E814 collaboration [31]. The experimental technique used in the E814 collaboration was quite immune to the nuclear background and the values obtained agreed well with theoretical cross sections. Table 1.1 shows the results obtained by Norbury [16] for semi-inclusive cross sections, compared with the E814

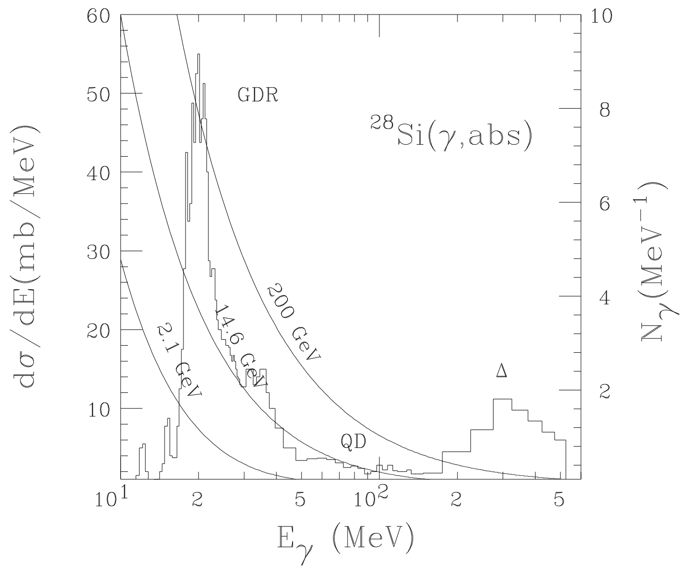

Figure 1.3: Photo-absorption cross section of the ^{28}Si nucleus. The virtual photon spectrum generated by the WW approximation for three different beam energies are also shown for comparison. Ref [6]

measurements. The uncertainties in the theoretical calculations arise from the measured uncertainties in the photo-nuclear data used in the calculation. The agreement between the theoretical calculations and the experimental measurements is not good for the Al target. This could be due to the effect of the nuclear component which can make a substantial contribution to the measured cross sections for low Z targets. The other significant feature in these data is that the neutron cross sections are higher and the proton cross sections are lower than the theoretical calculations (except for the Al target).

Table 1.1: Comparison of the measured (σ_{EXP}) and calculated (σ_{WW}) semi-inclusive cross sections at 14.6 GeV/nucleon beam energy.

Projectile	Target	Final State	$\sigma_{EXP}(mb)$	σ_{WW} (mb)
Si	Al	1p	37 ± 5	24 ± 2
Si	Al	1n	15 ± 4	9 ± 1
Si	Sn	1p	313 ± 4	317 ± 32
Si	Sn	1n	136 ± 6	118 ± 12
Si	Pb	1p	746 ± 27	806 ± 81
Si	Pb	1n	347 ± 18	301 ± 30

The charge dependence of EMD cross sections in heavy ion reactions has been investigated by Lissauer and Takai [18]. It has been shown that the Z_T^N dependence observed at the Bevalac with N=1.4 could be explained as a consequence of an "apparent" charge distribution. The apparent charge distribution in this context defines the special region where the projectile and the target interact only through EM forces. Figure 1.4 shows the measured Z dependence of EM cross sections for beam energies ranging from roughly 1 GeV/nucleon to about 200 GeV/nucleon. The dashed lines in the figure correspond to their calculations for the expected N dependence for three different minimum impact parameter values. It is clear from this plot that most of the observed deviations are consistent within the WW approximation.

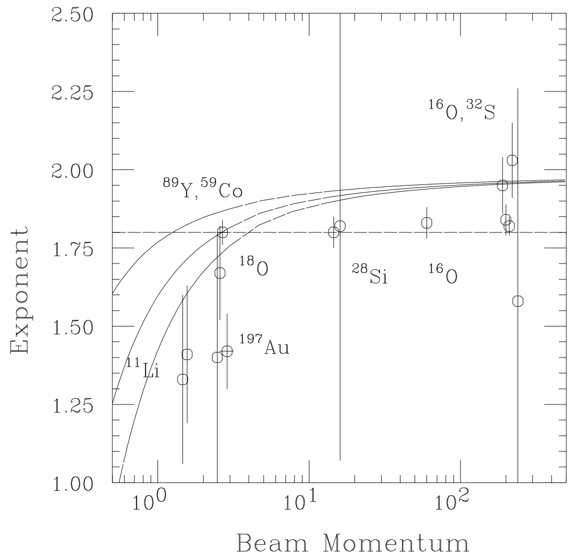

Figure 1.4: The charge dependence of the EMD cross section for different beam energies. The curves represent the theoretical calculations under the WW approximation. Ref [6]

2 Multipole Theory

The WW approximation is a very useful approximation used to understand electromagnetic processes. However, it breaks down in the regime of 100 MeV/nucleon energy due to the assumptions made in the derivation. The availability of new experimental measurements suggests the need for a theoretical model which can be used for a wide range of energies and all nuclei.

The virtual photon spectra consists of photons of different multipolarities. These multipolarities can be quite important at different beam momenta for the excitation of the GDR. An accurate theoretical analysis which involves the decomposition of the virtual photon spectra into its components was carried out by Bertulani and Baur [11]. These studies show that the analytical form of the WW essentially corresponds to photons of electric dipole (E1) multipolarity. Other important multipolarities include the electric quadruple (E2) and the Magnetic dipole (M1). However, it can be shown that at higher momenta, only one component, namely E1, is dominant.

The most important contributions to the cross section come from E1 and E2. We can write the EMD cross section for the one photon exchange as,

$$\sigma_{EMD} = \int \left[n_{E1}(\omega)\sigma_{E1}(\omega) + n_{E2}(\omega)\sigma_{E2}(\omega)\right] \frac{d\omega}{\omega}$$

where $\sigma_{E1}(\omega)$ and $\sigma_{E2}(\omega)$ are the photo-nuclear reaction cross sections for the electric dipole and electric quadruple resonances respectively. The quadrupole resonance consists of two modes, namely, the isoscalar and the isovector. The isoscalar resonance has not been observed with most of the light nuclei [6]. The E1 photon spectra is equal to the analytical form of the WW spectrum $n(\omega)$ given earlier in equation 1.1. The analytical form of the E2 spectra is given by [11]

$$n_{E2}(\omega) = \frac{2Z_T^2\alpha}{\pi\beta^4}\left[2(1-\beta^2)K_1^2 + \xi(2-\beta^2)^2K_0K_1 - \frac{\xi^2\beta^4}{2}(K_1^2 - K_0^2)\right] \qquad (1.2)$$

For a crude estimate of the response of the nucleus to the different multi-polarities, we can factor the $n_{Ei}(\omega)$ out of the integral and evaluate them at a single energy and use the sum rules [11] to evaluate $\int(\sigma_{Ei}(\omega)/\omega)d\omega$. This allows us to rewrite the equation as a function of the projectile mass and charge,

$$\sigma_{EMD} = 60\frac{n_{E1}(\omega_1)}{\omega_1}\frac{NZ}{A} + 0.22\times10^{-3}n_{E2}(\omega_2)\omega_2ZA^{2/3} \qquad (mb)$$

where ω_1 and ω_2 are the energies for the Dipole and the Quadrupole resonances respectively.

Figure 1.5 shows the contributions of E1 and E2 to the total EMD cross section as a function of the beam momentum. We can neglect the contributions from E2 at higher beam energies. But at low energies, the contribution can be as high as 50%. The reason for the failure of the WW at low energies where E2 is important can be shown by very simple arguments [11]. The E1 photons originate from the contraction of the target electric field. The higher the beam momentum, the higher the photon intensity due to the Lorentz contraction. The E2 photons originate from the non-uniformity of the field lines caused by the finite dimension of the projectile. Although this increases with the beam momentum, once the electric field lines are contracted and are in the plane perpendicular to the beam direction, the intensity remains almost constant.

A more accurate calculation of E1 and E2 has been performed by Norbury [16, 17] by using the experimental photonuclear cross sections for $\sigma_{E1}(\omega)$ and theoretical predictions for $\sigma_{E2}(\omega)$, and numerically evaluating the integral without removing the energy dependence of the photon spectra. The results, which are summarized

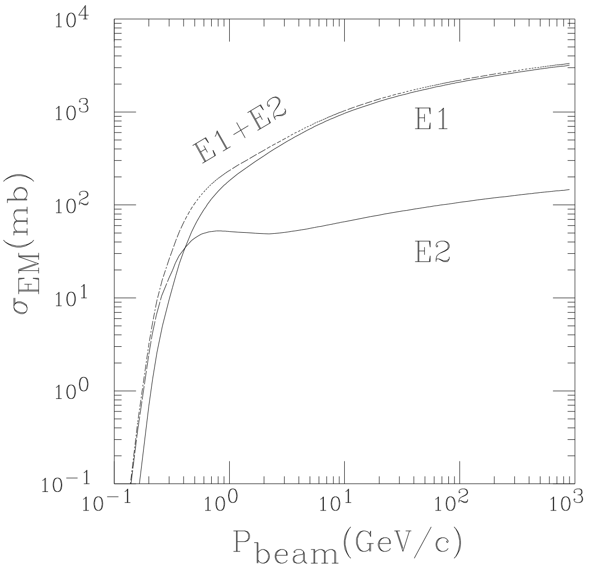

Figure 1.5: Effect of photon multipolarities at different beam energies. Ref [6]

in Table 1.2, indicate that above 10 GeV/nucleon, the WW approximation can be used successfully. The difference between the two ratios given in the table, arises essentially from the difference in the photonuclear cross section contributions used in the evaluation of σ_{WW} and σ_{E1}. These results clearly indicate the importance of the E2 contribution at beam energies below 2 GeV/nucleon.

3 Multi-photon Excitations

So far, due to its simplicity, the discussion has been limited to the absorption of a single photon. However, we can discuss the possibility of the absorption of more than one photon by the projectile (interaction with the same target nucleus) within the WW picture. This is formulated by Bertulani and Baur [11] and many others in the harmonic oscillator approximation where multiple photon excitation is treated as the multiple excitation of a pure harmonic oscillator. In the harmonic oscillator approximation, the differential cross section for the absorption of one photon of energy E^* is given by [19, 20],

$$\frac{d\sigma_1}{dE^*} = \int 2\pi b \; db \; e^{-m_\gamma(b)} \phi(E^*, b)$$

with

$$m_\gamma(b) = \int dE_\gamma N(E_\gamma, b) \sigma_\gamma(E_\gamma) = \int dE_\gamma \phi(E_\gamma, b)$$

Table 1.2: Calculated cross sections for a single neutron emission from ^{197}Au projectiles on ^{197}Au targets for different beam energies. Here σ_T represents the sum of the cross sections σ_{E1} and σ_{E2}.

Beam Energy	σ_{WW} (b)	σ_{E1} (b)	σ_{E2} (b)	σ_{WW}/σ_T	σ_{E1}/σ_T
100 MeV	0.56	0.53	0.83	41%	39%
300 MeV	1.7	1.6	0.8	71%	67%
500 MeV	2.3	2.2	0.7	79%	76%
2.1 GeV	4.9	4.7	0.6	92%	89%
12 GeV (AGS)	11.1	10.8	0.7	97%	94%
60 GeV (CERN)	19.3	18.7	1.0	98%	95%
200 GeV (CERN)	25.5	24.7	1.1	99%	96%
200 GeV (RHIC)	49.5	48.1	1.4	100%	97%

and

$$N(E_\gamma, b) = \frac{Z_T^2 \alpha}{\pi^2} \left(\frac{E_\gamma}{\hbar \gamma v}\right)^2 \left[\frac{c}{v}\right]^2 \left(K_1^2(\xi) + \frac{1}{\gamma^2} K_0^2(\xi)\right)$$

where $\sigma_\gamma(E_\gamma)$ is the total photo-absorption cross section, $\phi(E_\gamma, b) = N(E_\gamma, b)\sigma_\gamma(E_\gamma)$, and the probability of the absorption of a single photon of any energy with a given impact parameter b is $P_N(b) = (1/N!) m_\gamma^N(b) e^{-m_\gamma(b)}$. Similarly, the differential cross section for the absorption of two photons is,

$$\frac{d\sigma_2}{dE^*} = \frac{1}{2!} \int 2\pi b \, db \, e^{-m_\gamma(b)} \int dE_1 \phi(E_1, b) \phi(E^* - E_1, b)$$

The total cross section for the EMD upto two photon excitation is given by,

$$\sigma = \int dE^* \left[\frac{d\sigma_1}{dE^*} + \frac{d\sigma_2}{dE^*}\right]$$

These calculations can be extended to calculate the cross sections due to the absorption of any number of photons quite easily. Table 1.3 shows the results obtained by this method for multiple photon absorption up to 4 photon numbers [19, 20]. The experimental difficulty in observing a double GDR over a single GDR by measuring the total integrated cross sections is clear at this point since the double GDR cross sections are less than 1% of the single GDR cross sections. Conclusive experimental evidence of the existence of DGDR in electromagnetic dissociation has not been found yet. However, recent measurements with heavy projectiles (such as ^{136}Xe) indicate the possibility of observing DGDR in electromagnetic dissociation [21].

Table 1.3: Calculated cross sections for multiple photon absorptions.

Photon Number	^{16}O on ^{238}U at 100 GeV/nucleon	^{32}S on ^{238}U at 100 GeV/nucleon
1	2.5 b	4.3 b
2	20.6 mb	46.3 mb
3	328 μb	1.1 mb
4	4.8 μb	26.6 μb

C Scope of the Thesis

The original E814 proposal was submitted to the Brookhaven National Laboratory AGS committee in 1985 [25]. The main objectives of the peripheral collision program included the measurement of exclusive cross sections of electromagnetic dissociation channels up to several nucleons and the reconstruction of the excitation energy absorbed by the projectile when interacting with the target electromagnetic field. These measurements are necessary to test the theories behind the electromagnetic interactions. The scope of this thesis can be summarized as one step in achieving these goals.

During the intervening years, several experiments have reported valuable experimental measurements of the electromagnetic dissociation [1-5]. The first cross section measurements of the E814 results were published in 1990 [31], and there the dependence on Z_T and A_T was discussed. These cross sections show good agreement with the convolution of the WW spectrum with the experimental photonuclear cross sections. Other experiments also reported a similar dependence. However, satisfactory experimental observations of excitation energy measurements, which can provide invaluable information about the shape of the virtual photon spectrum, were not available until recently. Even today, only two measurements are available. The first report made by Olsen et al. [22] for the $^{16}\mathrm{O} \rightarrow 1\mathrm{p} + {}^{15}\mathrm{N}$ system is shown in Figure 1.6 at 2.1 GeV/nucleon energy. The peak at 9 MeV is due to the transitions to the ground state of the residual ^{15}N. The second peak which is about 5 MeV below the first peak is due to the transitions to the first excited state of ^{15}N which is in coincidence with 4 MeV γ rays corresponding to the de-excitation of the ^{15}N nucleus. The second measurement [32], reported for $^{28}\mathrm{Si} \rightarrow 1\mathrm{p} + {}^{27}\mathrm{Al}$ at 14.6 GeV/nucleon was a result of part of the work described in this thesis and will be explained here in detail.

The GDR in various nuclei has been studied through photonuclear reactions with a higher precision than that which can be achieved through high energy heavy ion reactions. However, at relativistic energies the properties of excited projectiles can be measured with a resolution that is good enough to probe their structure. In addition, heavy ion collisions can be useful in measuring the two photon excitation cross sections which are relatively small compared to single photon excitation cross

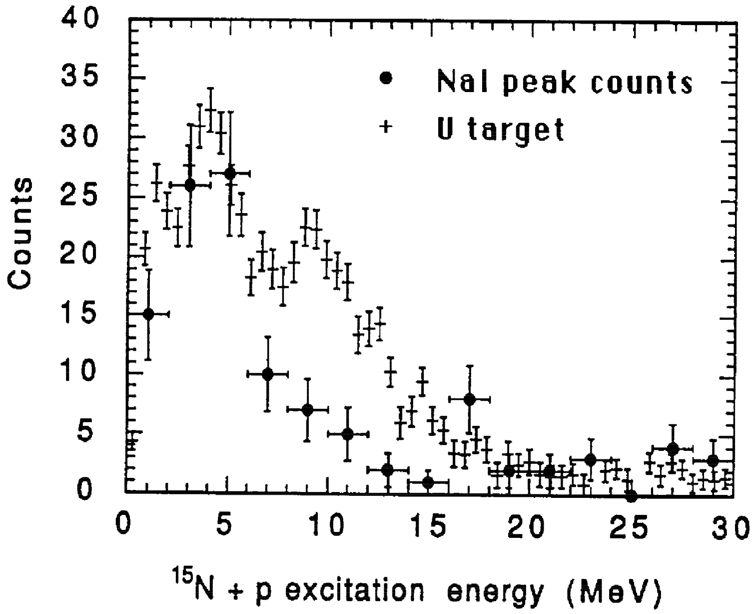

Figure 1.6: Measured excitation energy of the ^{16}O $\rightarrow$ 1p + ^{15}N reaction. Ref [22]

sections. This DGDR excitation mechanism can lead to new physics and even the production of new exotic nuclei [6].

The signatures of DGDR can be searched either through exclusive cross section measurements or by full excitation energy reconstruction, the latter being more promising. Bearing this in mind, the goals of the thesis were extended in both directions. As a result, new exclusive cross sections up to 5 nucleons in the final state including α and d particles were measured. In addition to the studies carried out with the 1p+^{27}Al channel, the excitation energy reconstruction of 1n+^{27}Si and 2p+^{26}Mg channels were carried out successfully. Although the two channels 1p+1n+^{26}Al and 2n+^{26}Si can be reconstructed using the methods discussed here, limited statistics discouraged us from carrying it out. However, the three reconstructed channels account for almost 70% of the total EMD cross section and hence permit useful comparisons with the $^{28}Si(\gamma, abs)$ data [23].

CHAPTER 2

The Experiment

Experiment E814 is a fixed target Relativistic Heavy-ion experiment operating in the Alternating Gradient Synchrotron (AGS) at Brookhaven National Laboratory. The collaboration of the experiment consists of about 50 physicists from ten different institutions. After the test runs in May 1987 and June 1988, data were taken in December 1988, June 1989, June 1990 and March 1991 with 14.6 GeV/nucleon ^{28}Si beams. The Peripheral Collisions program operated from 1988 to 1990 and results from the 1988 data were published [31]. Data from 1989 were used to study detector performances and other systematic effects. Data analyzed in this thesis were taken in 1990 with approximately 7 days of beam.

A Overview of the Experiment

1 Physics Programs

The original physics programs in E814 extend from the investigation of the properties of exotic nuclear systems produced by large impact parameter collisions to a study of energy flow and transparency by transition from large impact parameter collisions to small impact parameter collisions [25]. The program was later extended to study the properties of beam rapidity protons and neutrons (forward baryons) and to a search of strange matter which can form under high baryon densities and temperatures [26]. A description of the major programs operated during the last few years to study a broad range of topics in physics is given below.

1.1 Central Collisions

At AGS energies of 14.6 GeV/nucleon, small impact parameter collisions can produce higher hadronic densities which lead to new physical phenomena. Understanding of the reaction mechanisms possibly lead to the formation and evolution of new phases such as Quark Gluon Plasma [24]. However, even if a new state of matter is not found, systematic studies of stopping power and transparency will improve our understanding of nuclear-nuclear collisions. We measured the energy flow and the charged particle multiplicity, and their correlation with the forward baryons, with the data taken during the 1988 and 1990 runs [28, 29, 30]. Analysis of the 1991 data is still in progress.

1.2 Peripheral Collisions

The fragmentation of the projectile in large impact parameter collisions can be initiated by either the nuclear or the coulomb field of the target nucleus. These two processes can be distinguished by their dependence on the target mass and charge. The interaction of the projectile with the electromagnetic field of the target can be explained by the absorption of virtual photons [10, 11]. At AGS energies, the virtual photon flux is strong enough to produce multi photon excitations or even bound or quasi-bound multi-neutron states. With the E814 apparatus, exclusive cross section measurements as well as excitation energy measurements [31, 32, 33] can be done on channels which are very difficult to measure in low energy photo-absorption studies.

1.3 Strangelet Search

The high baryon rich matter can produce meta-stable or even stable exotic objects like strangelets which consist of up, down and strange quarks. Compared to normal matter, strangelets are heavier (mass number > 10 and Z/A range between 0.1 to 0.3) and have lifetimes in the order of 100 nsecs which are detectable in our spectrometer. The existence of strangelets could be important in verifying the existence of Quark Gluon Plasma since the Quark Gluon Plasma can be cooled down to form strangelets [34]. With the 1988 and 1989 data, we were able to set upper limits to light and heavy strangelet productions [35], and we expect to improve the limits with the analysis of data from the 1991 run. This program was later extended to measure particles that are composed of produced quarks such as $\bar{p}$ and $\bar{d}$ [36].

2 Detectors

The experimental setup used in June 1990 is shown in Figure 2.1. The coordinate system used in the experiment is defined by a right handed system with z along the incident beam direction and y vertical (upward). The detectors in the experiment consist of a beam telescope, a set of detectors in the target area to measure the energy and charged multiplicity and a set of detectors in the forward spectrometer to measure the position, energy and momentum of the final state particles. The two dipole magnets M1 and M2 which provide the deflection for the spectrometer, separate the detectors into two groups, namely the upstream detector group and the downstream detector group. A brief description of the detectors in these two groups are given below.

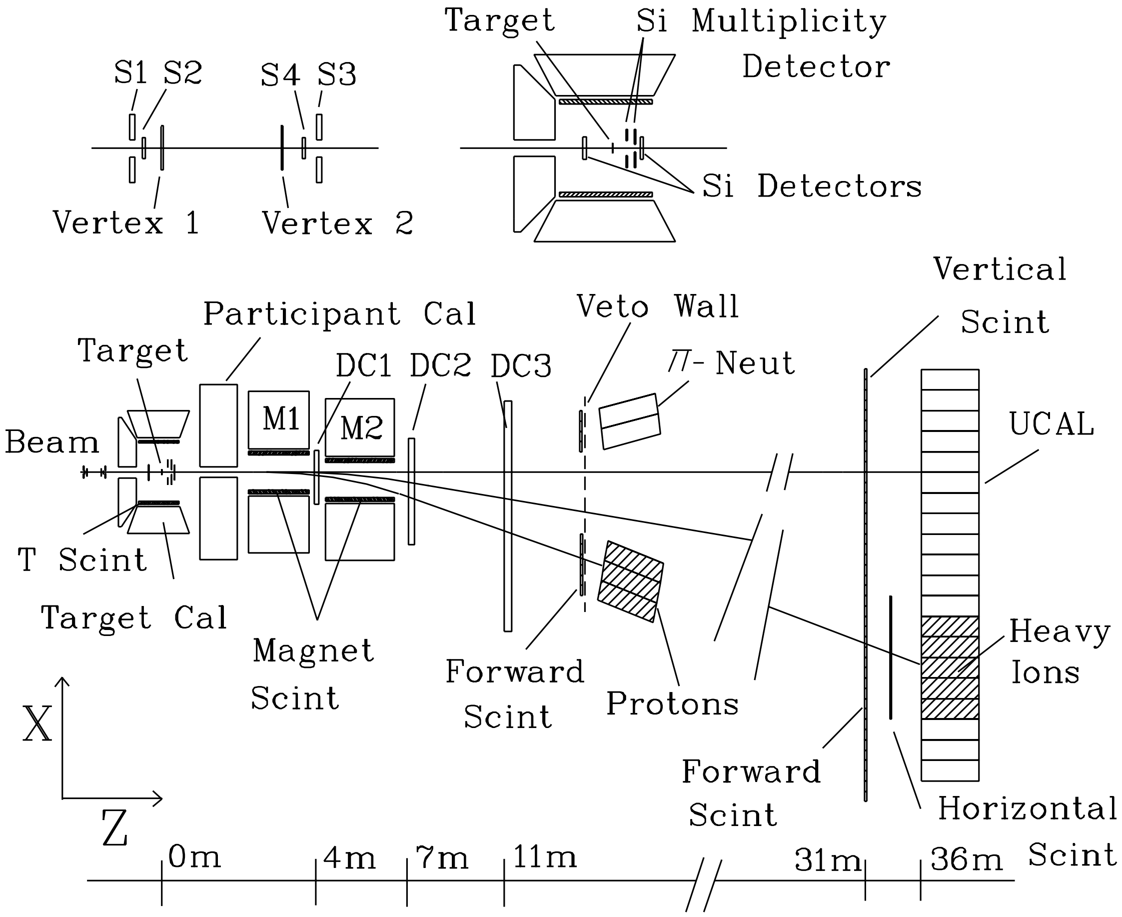

Figure 2.1: Diagram of the E814 apparatus. The beam enters through an aperture in the back of the target calorimeter. Forward going particles pass through the participant calorimeter opening and the two magnets M1 and M2. Track positions are measured in the tracking chambers DC1, DC2 and DC3. Charge is measured in the forward scintillators and energy is measured in the Target calorimeter, the Participant calorimeter and the U/Cu calorimeters. The top two figures show a blowup of the target region detectors.

2.1 Upstream Detector Group

- *Beam Telescope* (BSCI) – The beam telescope defines an acceptable beam particle for the experiment. It consists of two small scintillation counters (S2 and S4) and two veto counters with holes (S1 and S3). The timing signal T0 used as a start signal for the time of flight measurements was obtained from the S4 signals. The beam logic $S_2.S_4.\bar{S}_1.\bar{S}_3$ defines an approximately 3.0 mm beam spot on the target.

- *Beam Vertex Detector* (BVER) – The beam vertex detector consists of two silicon strip detectors of thickness 300 μm, placed in the incident beam line. They define the horizontal angle and position of the incident beam. The vertical strips have a pitch of 50 μm, and the two planes are separated by 3.0 m, giving an angular resolution of better than 20 μr.

- *Multiplicity Detector* (MULT) – The multiplicity detector consists of two concentric silicon discs, each 300 μm thick, and divided into 512 elements. The first disc is placed 3.4 cm downstream of the target and the second disc 8.2 cm downstream of the target. They cover an angular coverage of 2^o-40^o. These two detectors provide the charge multiplicity for any event.

- *Upstream and Downstream Si Detectors* – The upstream and downstream Si detectors consist of two surface barrier silicon detectors 1.0 cm in diameter and 100 μm thick. These are placed immediately upstream and downstream of the target to identify the charge of the incoming and outgoing particles.

- *Target Calorimeter* (TCAL) – The target calorimeter is composed of 992 NaI crystals, each of area 4x4 cm^2 and 6 radiation lengths thick, mounted in 5 separate boxes facing the target. Four of these boxes are placed with their faces parallel to the beam line (side walls) and the remaining box which contains a hole for the beam to pass, is positioned upstream of the target with its face normal to the beam line (back wall). This detector detects interaction products emitted at angles greater than 45^o up to almost 180^o.

- *Target Scintillators* (TPAD) – The target scintillators consist of 52 scintillators lining the inside face of the target calorimeter. This detector covers the same angular coverage as the target calorimeter side walls. This provides a measurement of charge multiplicity for any interaction. This measurement is complicated by the back scattered particles (albedos) from the TCAL.

- *Participant Calorimeter* (PCAL) – The participant calorimeter is a lead-scintillator calorimeter read out through wave-length shifting fibers into 512 photomultiplier tubes. It is divided into 16 azimuthal, 8 radial and 4 depth segments and has the same angular coverage as the multiplicity detector. This detector is used to measure E_T in central collisions. However, it also serves as an excellent veto against nuclear interactions in peripheral collision studies.

2.2 Downstream Detector Group

- *Magnet Scintillators* (MSCI) – The magnet scintillators consist of 16 scintillators which line the lateral walls of the spectrometer magnets. The two side walls of each magnet are covered almost completely by them (8 in each magnet, 4 on each side of each magnet). Scintillators in the magnets D8 and D9 are 3.7x120x1 cm^3 and 3.7x230x1 cm^3 respectively. These are used in the peripheral program to veto events originating from nuclear interactions.

- *Veto Wall* – The veto wall consists of a set of scintillation counters, placed above and below the beam line in a vertical plane at z=12 m. These counters are mounted sufficiently far from the horizontal plane to be in the shadow of the forward collimation system and are used to veto background events caused by interactions downstream of the magnets.

- *Tracking Chambers* (DRCH) – The tracking chambers consist of an interpolating cathode pad drift chamber DC1 located between the two magnets, with one single plane of two dimensional cathode pad readout, and two drift chambers DC2 and DC3, located downstream of the magnet. These two chambers are of identical design except for size and number of wires. They consist of a drift section as well as a pad section. All three chambers are designed and constructed to detect tracks originating from minimum ionizing particles as well as beam-like fragments.

- *Forward Scintillators* (FSCI) – The forward scintillation counters measure the charge, time of flight and vertical coordinate of forward going particles. They are grouped together and form two hodoscopes which are located downstream of the magnet at z=12 m and z=31 m respectively. The upstream hodoscope consists of 10 vertical scintillator plates of dimensions 9.5x1x60 cm^3 (6 of these are placed in the region of Z/A=1, and the remaining 4 are placed in the region of Z/A<0) and the downstream hodoscope consists of 39 vertical scintillator plates of dimension 10x1x120 cm^3.

- *Horizontal Counters* (HSCI) – The horizontal counters consist of a scintillation counter array consisting of 5 horizontal counters of dimensions 10x1x120 cm^3 placed at z=34 m. They are placed directly in the path of the deflected beam particles. These counters provide additional information on the charge measurement of the heavy ion fragments.

- *U/Cu Calorimeters* (UCAL) – Stacks of 25 U/Cu calorimeter modules were installed downstream of the magnet at two locations, z=13 m and z=36 m, to measure the energy and the position of reaction fragments at the downstream end of the spectrometer. Each module is approximately 20x100x120 cm^3 and they cover the same area as the forward scintillator hodescopes.

3 Trigger

3.1 Goals of the Trigger

The trigger system is a chain of electronics, which select the events to be recorded on magnetic tapes [37]. Due to the unknown nature of the characteristics of interesting events, the trigger was designed to permit as much flexibility as possible through software controlled logic systems. Every event is analyzed using a limited number of signals extracted from the detectors to allow the data acquisition system to select good events for recording on magnetic tapes for further analysis. It has the capability to enhance the rare event types by downscaling (i.e accepting only a fraction) the higher cross section events, as well as to record a variety of event types.

The main goals of the E814 trigger system for the three principal physics programs are:

- Identify central collisions through the requirement of high E_T using weighted analog sums of the signals from detectors in the target region, especially the participant calorimeter and the target calorimeter.
- Identify peripheral collisions through a requirement of low E_T in the target region, and appropriate energy and charge in the U/Cu calorimeters and forward scintillators.
- Identify candidates for strangelets through a measurement of time of flight in the forward scintillators by selecting low velocity particles in the final state.

To achieve these goals, summed signals from most of the detectors were made available at the trigger electronics, for decision making. This included signals from target region detectors as well as downstream detectors. Drift chambers were not included in the trigger, since track recognition was not required at the trigger level.

3.2 Trigger setup

First, signals from different detectors were grouped [1] together and brought to the counting house where the trigger electronics are set up Necessary time delays were added to the signals, depending on the location of the detectors as well as the stage at which the signals were processed in the trigger. All these signals were calibrated and gain equalized prior to the run. However, the gains of the photomultiplier tubes

[1] The formed groups of signals for important detectors are described in section B

show long term as well as short term variations. Hence, the detectors were calibrated throughout the run as often as was necessary for the proper operation of the trigger.

The trigger makes its decisions at three separate levels as shown in Figure 2.2. At the preliminary stage of the trigger (beam trigger), a decision is made as to whether a good beam particle has passed through the Beam Scintillator system. Then, the coincidence of the beam trigger and a prompt signal from one of the major detectors (multiplicity detector, U/Cu calorimeters, target calorimeter or participant calorimeter) was used to form the pre-trigger. The pre-trigger issues the START signals to all the ADC's and TDC's to start their digitization and activate the higher level triggers which process in parallel with the digitization. At the next level, the trigger (1st level) checks for the presence of another beam particle close to the one generated at the pre-trigger and rejects the event if such a particle exists (after protection). If not, the last stage (2nd level) will be activated and the decision is made as to which physics events are to be recorded, and the control is passed over to the data acquisition system.

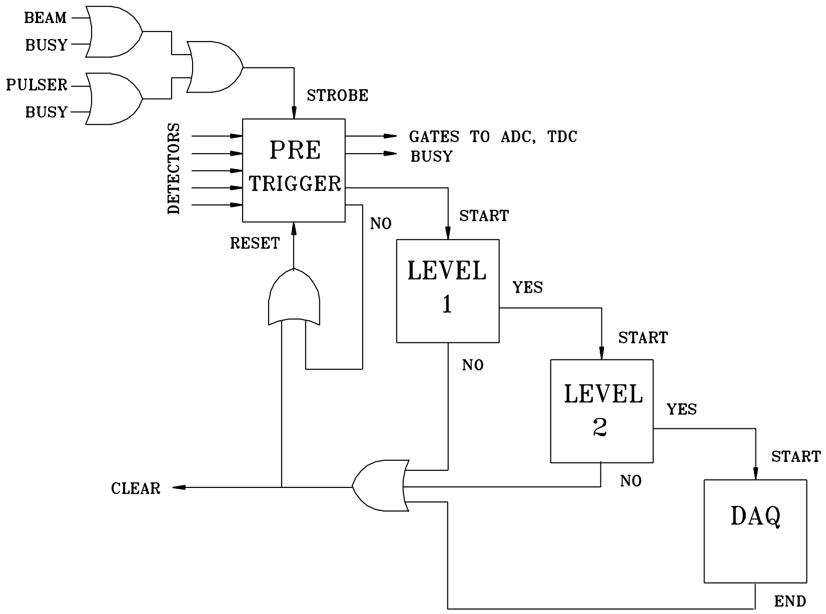

Figure 2.2: A block diagram of the E814 trigger system.

4 Data Acquisition System

4.1 Front End

The data acquisition system consists of 6 fastbus crates, each controlled by a SLAC Scanner-Processor (SSP) as shown in Figure 2.3. Five of these read out their own crates, and pass the data to the Master SSP, which reads out its own crate and assembles all the data into an event. The Master fastbus crate has a 4 MB fastbus memory module, a CFI card which connects to a Microvax and a Struck FBD to read the CAMAC branch which contains trigger electronics and a portion of data from several detectors.

After receiving a START signal from the trigger the Master SSP takes the following actions.

- A logic output signal (SSP BUSY) is generated which suppresses any triggers, until it is cleared.
- The lower level SSPs are signaled to begin reading out the modules in their crates. Each crate works in parallel.
- Devices in the master crate are then read out.

When the Master SSP is finished with its own crate, it begins polling the lower level crates for their data, and builds the data record for one event. This event record is then written into the memory card and SSP BUSY is cleared.

During a spill, the event records are stored in the Fastbus memory, and when the spill is over, the microvax is given the signal to read before the next spill occurs. If the microvax does not finish reading in time, the next spill or spills are skipped until it is done. On average 30 events per spill will be recorded and the SSP readout time is approximately 10 msec per event.

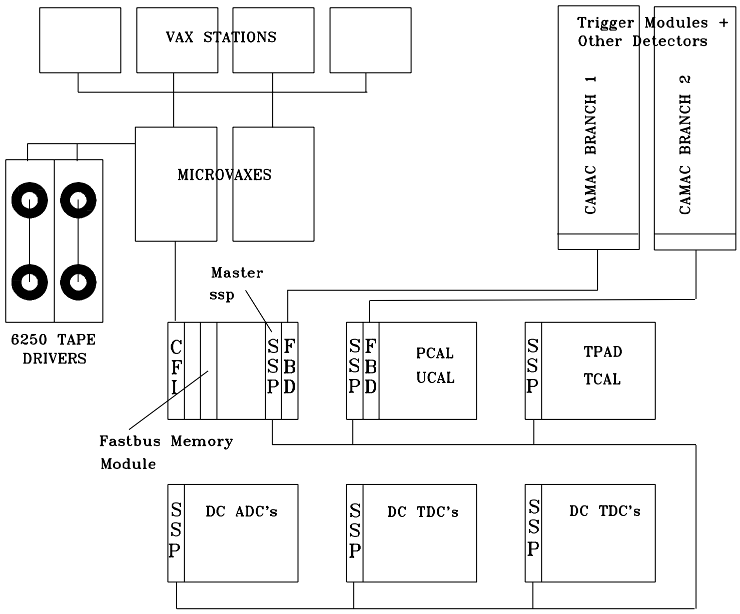

Figure 2.3: A block diagram of the E814 data acquisition system.

4.2 Microvax

The heart of the data acquisition system is a Microvax which is linked to the Master SSP via the CFI controller. This machine is connected to two, high speed, 9 track tape drives, on which data is written. It is also connected via DECnet (Ethernet lines) to another Microvax and 4 Vaxstations.

Data collection is done by three processes:

- The Link server, which waits for a signal from the Master SSP, reads out the fastbus memory card, and stores events into a buffer.
- The Buffer logger, which writes events to a tape, if the user desires.
- The Buffer processor, which takes events and puts them into the event pool, which is a large, shared memory area that user-written programs may pull events from. Typically, this receives about 10% of the events.

In addition, there are processes (Daq servers) which get events from the pool, and transmit them, via DECnet, to Vaxstations which perform online monitoring of data. On each workstation, another process (the Daq client) collects events from the Daq server, and puts them into an event pool local to the workstation. Typically, the experimenter runs programs (consumers), which extract events from this pool and analyze them.

B Detectors used in EMD studies

Although we used all the detectors in the experiment for EMD studies, in this section an extended description of three of the most vital detectors is given. These detectors are used to measure the charge, energy and momentum of the fragments in the downstream end of the spectrometer.

1 Forward Scintillators

1.1 Construction

The principal objectives of Forward Scintillation counters are to measure the charge (Z), the time of flight (T) and the vertical position of the reaction fragments at the downstream end of the spectrometer. They must have the capability to measure Z=1 as well as Z=14 particles requiring a dynamic range of 1:200. In addition, the online Z measurement should be good enough to be used in the second level trigger.

The resolution in the measurement of Z in a scintillator depends primarily on the statistical fluctuations in the deposited energy arising from the production of energetic δ rays, and the non-uniformity in thickness over the exposed area of the scintillator material. The general theory for the loss of energy of charged particles in matter is known to be a Landau distribution [38]. The limited energy deposited by the ionization of heavy particles in thin absorbers due to finite thickness was first discussed by Vavilov [39] and was later improved by Badhwar et al [40, 41] correcting for the energy loss due to escaping electrons. This effect makes the distribution more Gaussian in shape because the statistical fluctuations have less effect on the mean energy deposition. If we approximate the distribution of the deposited energy analyzed by Badhwar for heavily ionizing particles by a Gaussian distribution, it can be shown that,

$$\left(\frac{\sigma}{I}\right)^2 = \frac{\gamma S}{(2SZ^k)^2}$$

where S is the scintillator thickness, k is a property of the scintillator and I is the mean light yield. γ is given by

$$\gamma = \xi\epsilon_D\left[2 - \frac{\epsilon_D}{\epsilon_{MAX}}\left(\frac{\beta^2}{2} + 1 + \beta^2\ln(\frac{\epsilon_{MAX}}{\epsilon_D})\right)\right]$$

where $\xi = 0.3(z/A)(mc^2/\beta^2)SZ^2$.

In these expressions ϵ_D is the mean energy deposited by a δ ray that leaves the scintillator and ϵ_{MAX} is the maximum δ ray energy. The quantities z and A are the atomic number and the atomic weight of the absorber respectively, m is the electron mass, and βc is the particle velocity. For a 1 cm thick scintillator, we find that $(\sigma/I) = 0.18/Z^{(k-1)}$ which yields a resolution of 2.8% at Z=14, assuming k=1.7.

In addition to the effects discussed above, the measured Z resolution of a light output of a scintillator suffers due to the scintillator saturation as well as the gain drifts in photomultiplier tubes. These questions are addressed in more detail in chapter 3.

The NE104 scintillators with 120 cm attenuation length were selected to construct the downstream forward scintillators because of their faster decay time properties. The upstream scintillators were constructed with Bicron 420 scintillators. Each scintillator slat was connected to two photomultiplier tubes as shown in Figure 2.4. Light generated in the scintillator material was guided into the phototubes through light guides connected between the cathode of the phototube and the scintillator material itself. We used EMI-9954 photomultiplier tubes with 12 stage bases in most of the forward scintillators.

From the downstream scintillators, two signals were taken from each phototube, one from the anode and the other from the last dynode. The last dynode signals were added together and inverted and this signal was brought into the FERA ADC's (LeCroy 4300B, Fast Encoding Readout ADC) of 10-bit accuracy, and was used in the trigger. The anode signals were split passively between a fastbus ADC (LeCroy 1885F dual range ADC) and a dual discriminator (Phillips Model 7106). One output of the discriminator was fed to a TDC (LeCroy Model 4291B) of 300 ps/channel resolution and the other was connected to a FERET (LeCroy 4303, Fast Encoding

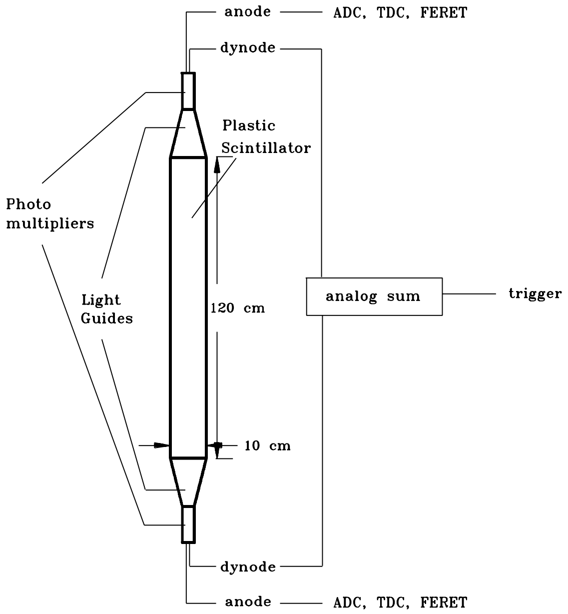

Figure 2.4: A forward scintillator slat.

Readout TDC) with 50 ps/channel resolution which was used in the trigger. The dual range ADC's lower range has a 50 fC/channel sensitivity whereas the upper range has 400 fC/channel, giving a full digitizing range of $\approx$ 1600 pC/channel. These ADC's are extremely useful in maintaining the required sensitivity along the full dynamic range.

The anode signals of the upstream scintillators follow the same path as those of the downstream scintillators, but the dynode signals are discriminated immediately after extraction from the phototube to prevent the degrading of the timing resolution due to the change in the pulse shape when the signals pass through long delay cables. The output signals of the discriminators were brought into the counting house and discriminated again and connected to a 50 ps/channel TDC (LeCroy Model 2280A) system for a timing measurement of higher precision.

1.2 Calibration

The gain equalization of each phototube was done by using a ^{106}Ru, 1 mC radio-active source. First, the Ru source was mounted on a holder and placed at right angles to the scintillator slat, roughly, in the middle. Another small scintillator counter with one phototube attached, was placed behind the counter to be calibrated. This counter serves as a trigger for the signals from the Ru source to reduce the background due to cosmic rays (as well as x-rays and γ rays emitted by the Ru source). Signals from dynodes were connected to an ADC with the gates generated by the trigger counter and read by a small data acquisition system controlled by a PC. One phototube at a time was calibrated to bring minimum ionizing particles roughly at 300 ADC counts